The Astronomical Journal, 153:13 (5pp), 2017 January doi:10.3847/1538-3881/153/1/13

SPATIALLY RESOLVED SPECTROSCOPY OF EUROPA'S LARGE-SCALE COMPOSITIONAL UNITS AT 3–4 μm WITH KECK NIRSPEC

P. D. Fischer[1], M. E. Brown[1], S. K. Trumbo[1], and K. P. Hand[2]
[1] Division of Geological and Planetary Sciences, California Institute of Technology, Pasadena, CA 91125, USA; pfischer@caltech.edu
[2] Jet Propulsion Laboratory, California Institute of Technology, Pasadena, CA 91109, USA
Received 2016 July 6; revised 2016 October 12; accepted 2016 November 4; published 2016 December 20

ABSTRACT

We present spatially resolved spectroscopic observations of Europa's surface at 3–4 μm obtained with the near-infrared spectrograph and adaptive optics system on the Keck II telescope. These are the highest quality spatially resolved reflectance spectra of Europa's surface at 3–4 μm. The observations spatially resolve Europa's large-scale compositional units at a resolution of several hundred kilometers. The spectra show distinct features and geographic variations associated with known compositional units; in particular, large-scale leading hemisphere chaos shows a characteristic longward shift in peak reflectance near 3.7 μm compared to icy regions. These observations complement previous spectra of large-scale chaos, and can aid efforts to identify the endogenous non-ice species.

Key words: planets and satellites: composition – planets and satellites: individual (Europa) – planets and satellites: surfaces

Supporting material: data behind figure

1. INTRODUCTION

Much of Europa's surface composition remains to be determined. The identities of the native non-water-ice species are of special interest because they can inform knowledge of Europa's subsurface environment and geochemical evolution. Reflectance spectroscopy of the surface at 3–5 μm is currently limited, and may help to resolve this puzzle.

Most reflectance spectra of Europa at 3–5 μm was acquired by the Galileo NIMS (Near Infrared Mapping Spectrometer) investigation, which detected several non-water-ice surface species at the hemisphere scale, including hydrogen peroxide at 3.5 μm (Carlson et al. 1999), CO_2 at 4.25 μm (McCord et al. 1998; Hand et al. 2007) and possibly SO_2 at 4.0 μm (Hansen & McCord 2008). However, NIMS investigations at these wavelengths were hindered by the radiation environment at close distances to Europa, limiting data quality and high spatial resolution investigations. Initial detections of peroxide (H_2O_2), CO_2, and SO_2 were obtained at longer distances from Europa with only hemisphere-scale resolution (Smythe et al. 1998). NIMS 3–5 μm investigations with spatial resolution are limited to the work of Hansen & McCord (2008), though the data are low quality. Earth-based observations at 3–5 μm are also limited; pre-Galileo investigations resolved little spectral structure past 3 μm, leading to various spectral interpretations (e.g., Pollack et al. 1978; Lebofsky & Feierberg 1985; Spencer 1987). Recent ground-based observations by Hand & Brown (2013) have added to these data, obtaining high-quality 3–4 μm hemispherically resolved spectra and localizing peroxide to the leading hemisphere.

Ground-based observations using adaptive optics (AO) can combine high-quality spectra with coarse spatial resolution, resolving large-scale geological and compositional units, with the potential for significant improvements to previous work. The geographic distribution of surface species is important because it can reveal endogenous or exogenous sources through association with geologic or external processes. One key target for such observations is large-scale chaos, young regions of widely disrupted terrain indicating interaction with the subsurface (e.g., Lucchitta & Soderblom 1982; Carr et al. 1998; Collins & Nimmo 2009). Chaos regions are likely the most direct link to the subsurface environment and endogenous composition.

Here we present the first ground-based AO spectroscopic observations of Europa at 3–4 μm. These observations spatially resolve east–west and north–south slices at a scale of several hundred kilometers and focus on distinct large-scale compositional regions, including the trailing hemisphere bullseye, the leading hemisphere large-scale chaos units, and the leading hemisphere upper latitudes. These spectra show clear variations across the surface and between these compositional regions, and can aid future efforts to identify Europa's native salts.

2. OBSERVATIONS

The anti-Jovian, sub-Jovian, and leading hemispheres of Europa were observed on 2013 December 27, 2016 February 24, and 2016 February 25, respectively. Observations were obtained with the near-infrared spectrograph instrument NIRSPEC (McLean et al. 1998) and adaptive optics (AO) system on the Keck II telescope. The spectrograph was set to the $3\farcs96 \times 0\farcs072$ slit in low-resolution mode ($R = 2000$) at the L band wavelengths of approximately 3.14–3.98 μm. The exact wavelength range varied by ~0.01 μm between different nights and during the night of 2016 February 25 after switching between high and low-resolution mode. All data reduction was performed with custom Python routines, and used the packages Astropy (Astropy Collaboration 2013) for working with fits files and skimage.transform (van der Walt et al. 2014) for curvature rectification. For wavelength calibration, we use an atmospheric transmission spectrum produced by ATRAN (Lord 1992). For telluric calibration on 2013 December 29, we observed HD 54371, a $V = 7.1$ G6 star at $3\fdg2$ separation from Europa, and on 2016 February 24–25, we observed HD 98947, a $V = 6.9$ G5 star at $1\fdg2$ separation from Europa. Each Europa pointing consisted of thirty 20 s coadds, and each

Table 1
Summary of Geographically Unique Europa Observations

UT Date	Hemisphere	Slit Orientation	Total Exp. Time (min)	Center Longitude	Center Latitude	Airmass Range	Telluric Calibrator
2013 Dec 27	anti-Jovian	E/W	40	195 W	4 N	1.02–1.18	HD 54371
2013 Dec 27	anti-Jovian	E/W	20	195 W	24 S	1.10–1.12	HD 54371
2016 Feb 24	sub-Jovian	E/W	120	338 W	0 N	1.10–1.75	HD 98947
2016 Feb 24	sub-Jovian	N/S	80	347 W	2 S	1.04–1.07	HD 98947
2016 Feb 24	sub-Jovian	N/S	20	352 W	2 S	1.06–1.07	HD 98947
2016 Feb 25	leading	E/W	40	79 W	0 N	1.24–1.38	HD 98947
2016 Feb 25	leading	E/W	40	82 W	15 S	1.11–1.18	HD 98947
2016 Feb 25	leading	E/W	40	95 W	1 S	1.08–1.14	HD 98947
2016 Feb 25	leading	N/S	40	86 W	2 S	1.04–1.08	HD 98947
2016 Feb 25	leading	N/S	40	101 W	2 S	1.30–1.47	HD 98947

telluric calibrator pointing consisted of one 12 s or 20 s coadd or two 15 s coadds. Each observation consists of two or four pointings, where the target was dithered between opposite ends along the slit in an AB or ABBA pattern.

We obtain precise viewing geometry and ephemerides from JPL Horizons. At the time of observations, the diameter of Europa subtended approximately 1″ or 10 resolution elements at the diffraction limit of the Keck telescope at 4 μm. The slit width of 0.″072 with AO is comparable to the Keck diffraction limit of 0.″10 at 4 μm. This diffraction-limited resolution corresponds to a spatial resolution of 300 km at the sub-observer point on Europa. We align the slit at either an east–west or north–south orientation with respect to Europa using the north pole position angle obtained from JPL Horizons. We average exposures to increase the signal-to-noise ratio (S/N) if the slit positions on Europa overlap and Europa's rotation between observations is negligible. This yields nine slit positions with unique geographic locations, summarized in Table 1.

3. ANALYSIS

The goal of this work is to measure the 3–4 μm reflectance spectra of Europa's major compositional units that are resolvable from the ground with adaptive optics. As found in Fischer et al. (2015), these units correspond to the trailing hemisphere, leading hemisphere upper latitudes, and leading hemisphere large-scale chaos regions. For this third unit, we focus on Western Powys Regio and Tara Regio as mapped by Doggett et al. (2009), which were well resolved at 1.5–2.4 μm in Fischer et al. (2015). Two additional chaos regions centered at 180 W and 0 W were found to be of similar composition by Fischer et al. (2015). We choose not to focus on these two chaos regions here because they border the trailing hemisphere unit and the longer wavelengths of these observations degrade the spatial resolution by a factor of two, causing more spatial contamination in the spectra.

After the basic data reduction described in the previous section, we extract the regional spectra as follows. Each SCAM guide camera image of Europa and the overlying slit is used to estimate the coordinates of the slit on Europa and the section of the slit corresponding to the geographic regions of interest. We digitally align each SCAM image to an orthographic basemap projection produced with the Python Basemap package. The size of Europa in pixels in NIRSPEC/AO (hereafter, NIRSPEC) and the SCAM/AO guide camera (hereafter SCAM) is calculated with detector resolutions of 0.″013 pixel^{-1} and 0.″0168 pixel^{-1}, respectively, and the angular diameter of Europa at the time of observation, which is 1.″02 or 0.″97 for the 2013 or 2016 observations, respectively. This gives diameters of 61 or 57 SCAM pixels and 79 or 74 NIRSPEC pixels for the 2013 or 2016 observations, respectively. We then cross-correlate and extract each 2D spectrum corresponding to the size of Europa in NIRSPEC. Each extracted 2D spectrum is individually normalized to a lambertian surface using the derived slit coordinates and the sub-solar coordinates from JPL Horizons. We restrict our analysis to slit positions with Lambertian corrections $\leqslant$2, which limits the phase angle to a maximum of 60°. To achieve higher S/N spectra, we combine identical observations, where the slit positions are nearly overlapping and Europa's rotation between exposures is negligible. This yields nine slit positions with unique geographic locations, summarized in Table 1. The uncertainty of these slit position coordinates on Europa is dominated by angular diffraction and varying placement of the slit on the disk between pointings. The diffraction-limited angular resolution of Keck at 4 μm is 0.″10, and overlapping slits were separated by up to approximately 0.″05. We estimate the uncertainty in aligning SCAM images to the orthographic projection as one SCAM pixel or 0.″017, which is small in comparison. Our results and conclusions are not sensitive to these uncertainties.

We extract spectra for surface regions by selecting the section of the slits spatially overlapping with the region of interest. These spectra are shown in Figures 1 and 2; they are not absolute flux calibrated but are calibrated relative to each other, and have been scaled inexactly for agreement between the NIRSPEC leading hemisphere spectra and the NIMS leading hemisphere spectrum of Carlson et al. (2009). We also show H- and K-band spectra from the OSIRIS data set of Brown & Hand (2013) and Fischer et al. (2015). We normalize the OSIRIS data set to a Lambertian surface and extract spectra overlapping with the NIRSPEC slit positions, which gives a good geographic match for H-, K-, and L-band spectra in each region of interest. These spectra are available through data behind the figure.

Three characteristic features of the L-band regional spectra, as discussed in the following section, are the amplitude and wavelength of the 3.6–3.8 μm peak and absolute reflectance. We map these features across all slit observations in Figure 3. For each spatial slit column, we calculate a unique spectrum as the mean of that spatial column and the four nearest spatial columns, which oversamples the diffraction-limited angular resolution by a factor of two. We quantify the amplitude of the 3.7 μm peak as a ratio of peak reflectance near 3.7 μm to

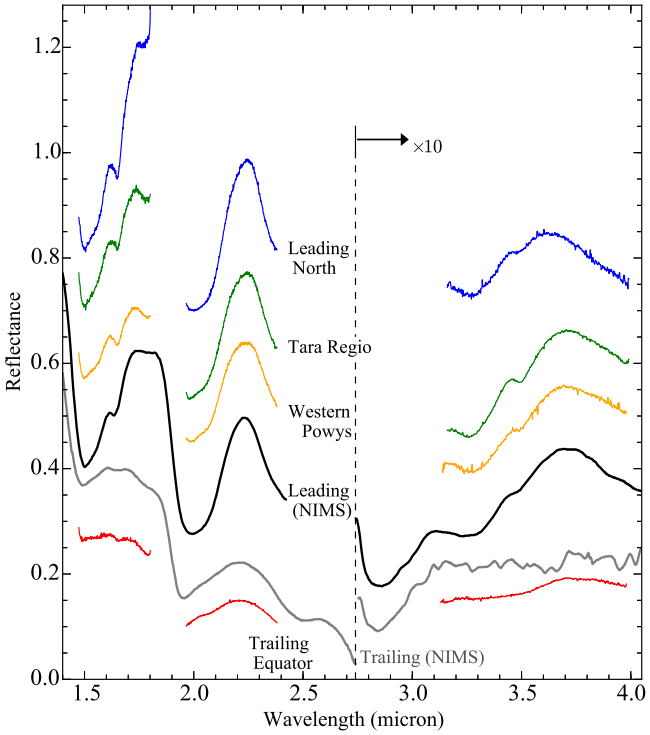

Figure 1. NIRSPEC L-band and OSIRIS H- and K-band spectra of large-scale compositional regions, and NIMS leading and trailing spectra digitized from Carlson et al. (2009) in black and gray. These are the first high-quality spatially resolved L-band spectra of Europa's surface, and show distinct variations among large-scale compositional regions. The trailing hemisphere is in red, leading hemisphere northern latitudes are in blue, and the chaos regions Western Powys Regio and Tara Regio are both in green to indicate similarity. For clarity, the L-band spectra are multiplied by 10, and the NIMS Leading, Western Powys, Tara Regio, and Leading North are shifted vertically by 0.15, 0.28, 0.35, and 0.58, respectively. These four regional spectra are available through Data behind the figure. The data used to create this figure are available.

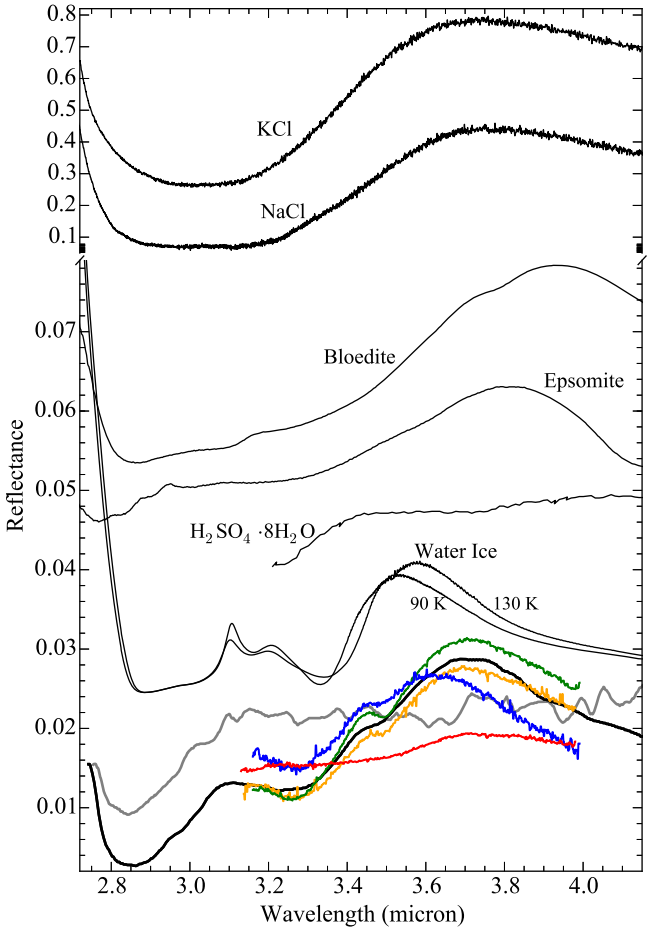

Figure 2. L-band spectra from Figure 1 and representative laboratory spectra of major hypothesized surface compositions. Observed spectra are the same color scheme as Figure 1, with no offsets. Sulfuric acid octahydrate is from Carlson et al. (2009). Blödite and epsomite spectra are from the USGS spectral library (Clark et al. 2007). NaCl is an irradiated evaporite and KCl is irradiated anhydrous grains at 100 K from K. P. Hand et al. (2016, in preparation). Water ice spectra at 90 and 130 K are derived using optical constants from Mastrapa et al. (2009) and the spectral modeling approach of Hapke (1981) with a grain size of 20 μm. For comparison, blödite is shown scaled by a factor of 0.4, and blödite and epsomite are shifted vertically by 0.05 and 0.044.

continuum reflectance near 3.25 μm, longward of the H_2O ice Fresnel reflectance feature. We find the wavelength of the 3.7 μm peak by fitting a Gaussian curve to the spectra between 3.55 and 3.85 μm and using the peak wavelength of the fitted Gaussian. We find the wavelength of the 3.25 μm continuum by Gaussian smoothing the spectra and finding the minimum value between 3.2 and 3.4 μm. The ratio map (Figure 3, top) is the ratio of the reflectance at these two wavelengths, where the reflectance values are the median-average of a 30 nm wide bin centered on these wavelengths. The absolute wavelength map (Figure 3, middle) is the derived wavelength of the 3.7 μm peak, and the mean reflectance map (Figure 3, bottom) is the mean reflectance value between 3.15 and 3.95 μm.

4. RESULTS AND DISCUSSION

Europa's NIR surface reflectance resembles the spectrum of water ice, but with asymmetric and shifted bands and a distinct continuum shape. These differences are not solely explained by variations in grain size, temperature, or crystallinity of pure water ice. Spacecraft images also show color and albedo variations that cannot be attributed to water ice, particularly associated with chaos regions and linea (e.g., Hand & Carlson 2015). The case is sound for sulfuric acid as the dominant non-water ice component on the trailing hemisphere (e.g., Carlson et al. 2009). However, the dominant leading hemisphere hydrate, causing the visible coloration in large-scale chaos, remains unclear.

L-band spectra of Europa's large-scale compositional regions can help to resolve this puzzle. These compositional regions are the trailing hemisphere, leading hemisphere upper latitudes, and leading hemisphere large-scale chaos (e.g., Fischer et al. 2015). At 3–4 μm each region shows a peak in reflectance near 3.7 μm (Figures 1, 2), decreasing to reflection minima in the 3 μm and 4.5 μm bands corresponding to the fundamental modes of water ice. The leading hemisphere spectra show an increase in reflectance near 3.2 μm attributed to Fresnel reflection, with a flattened shape more consistent with amorphous ice than crystalline ice. The trailing hemisphere spectrum is flatter than the leading hemisphere spectra, with a muted 3.7 μm peak and no apparent Fresnel reflection. The structure between 3.1 and 3.2 μm in the trailing hemisphere spectrum is distinct from the other spectra, and resembles a shifted and muted Fresnel reflection feature at 3.2 μm, or possibly a wide absorption feature extending from 3.2 μm to shorter wavelengths. Future observations with spectral coverage to 3 μm can further investigate this. The

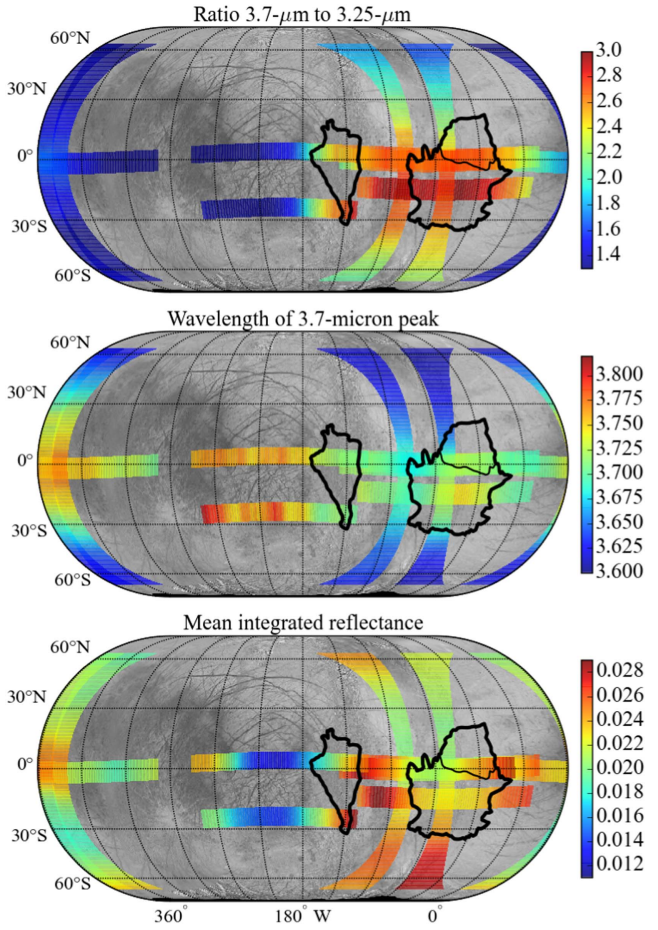

Figure 3. Maps of diagnostic L-band spectral signatures across spatially unique NIRSPEC observations. Top: reflectance ratio of peak near 3.7 μm to continuum near 3.25 μm, as a proxy for amplitude of 3.7 μm peak. Middle: absolute wavelength of 3.7 μm peak. Bottom: mean reflectance from 3.15 to 3.95 μm. Black outline near 150 W is Western Powys Regio and near 90 W is Tara Regio, mapped approximately from Doggett et al. (2009). The thin boundary near 90 W separates Tara (south) from an unnamed region mapped as lenticulated terrain (north), which shows the same yellow color as Tara chaos in Galileo SSI images and likely has a similar composition. (Basemap credit: USGS)

only non-water ice feature at the resolution and S/N of our observations is at 3.5 μm, attributed to peroxide (Carlson et al. 1999) and localized to the leading hemisphere (Hand & Brown 2013). We will explore the spatial distribution of peroxide and implications for exogenous composition in future work.

We further focus on the 3.7 μm peak because it is a discriminating feature of the observed spectra. The 3.7 μm peak is a continuum feature located between two absorption bands, which are likely the fundamental ν_1 and ν_3 stretch modes (3 μm) and ν_2 bending mode (4.5 μm) of water ice (e.g., Ockman 1958; Carlson et al. 2009), though the 4.5 μm absorption in sulfate may also contribute to the observed spectra. Interestingly, the amplitude of the 3.7 μm peak is qualitatively weaker in the more pure ice regions of the surface and stronger in the chaos region spectra, unlike the 1.8 and 2.2 μm water ice peaks (Figure 1). The wavelength of the 3.7 μm peak is also shifted to longer wavelengths in the chaos regions than in the icy polar regions. The amplitude of the 3.7 μm peak or 3 μm band is known to vary with grain size, where the amplitude increases for smaller grains when the band is saturated (e.g., Emery et al. 2005). However, the wavelength shift of the 3.7 μm peak to longer wavelengths in the chaos regions cannot be attributed to grain size. This peak wavelength shift does occur with changing temperature in pure water ice (e.g., Mastrapa et al. 2009; Clark et al. 2012), though pure water ice likely cannot produce the magnitude of this shift ($\sim$0.1 μm) or the absolute wavelength. For example, Figure 2 shows spectra of water ice at 90 K and 130 K, which is a reasonable dayside temperature range (e.g., Moore et al. 2009). These spectra peak at 3.53 and 3.58 μm respectively, whereas the icy leading north spectrum peaks at 3.62 μm and the chaos region spectra peak at 3.71 μm. Peak wavelengths near 3.6 μm are similar to spectra of icy regions on Enceladus (e.g., Brown et al. 2006) and Saturn's rings (e.g., Nicholson et al. 2008), two locations of nearly pure water ice. This suggests that the endogenous hydrate or salt associated with chaos regions is characterized by a stronger 3 μm band or weaker 4.5 μm band relative to pure water ice. This observation is similar to that for Callisto by Pollack et al. (1978), who claim that the strength and width of the 3 μm fundamental is deeper and broader in bound water ice than pure water ice, regardless of the non-ice composition. Detailed spectral modeling investigations in the region of the 3 μm band may provide further insight to Europa's native salts, but first more laboratory studies are needed to obtain low temperature reflectance spectra and optical constants of candidate materials, particularly salt–ice mixtures. The effects of Europa's external environment on reflectance spectra such as dehydration and irradiation must also be explored.

Spatial distributions of spectral signatures can provide further insight. We map three distinguishing characteristics of these spectra: the amplitude of the 3.7 μm peak, wavelength of the 3.7 μm peak, and mean L-band reflectance. These maps are shown in Figure 3, and reveal clear latitudinal and hemispherical variations. The ratio map (Figure 3, top) is the most spatially coherent, showing the strongest 3.7 μm peak amplitude at the leading hemisphere equatorial latitudes, decreasing in amplitude uniformly outward. This distribution is consistent and anti-correlated with global patterns of electron irradiation (Dalton et al. 2013) and sputtering rate (Cassidy et al. 2013). This at first suggests a simple grain size interpretation, in which irradiation amorphizes water ice producing larger grain sizes and weaker 3 μm bands. However, this trend is not true for the 1.5 and 2 μm bands, and a simple grain size interpretation does not take into account the compositional diversity apparent in Galileo SSI color images (e.g., Hand & Carlson 2015). This spatial distribution is not obviously correlated with large-scale chaos regions, two of which are outlined. However, such a correlation is difficult to distinguish with slit spectroscopy near the limit of the necessary spatial resolution and incomplete surface coverage. Even so, this spatial distribution is certainly distinct from that of water ice, which is most abundant in the leading hemisphere upper latitudes. The spatial distribution of the peak wavelength (Figure 3, middle) also trends toward longer wavelengths at lower latitudes. The peak wavelengths are longest in the anti-Jovian/trailing hemisphere quadrant, likely influenced by exogenous processing. The trend is weaker though clearly present on the leading hemisphere, where the effects of exogenous processing are less important. The longest peak wavelengths on the leading hemisphere are localized to Tara Regio, consistent with the hypothesis that the native non-ice species associated with chaos regions is characterized by a

broader 3 μm band. Finally, the mean reflectance (Figure 3, bottom) generally correlates with visible albedo, and the correlation is apparently reversed between leading and trailing hemispheres: on the trailing hemisphere, the L-band reflectance brightens on the visibly dark large-scale chaos regions, and on the leading hemisphere the L-band reflectance darkens on the visibly dark chaos regions. (Note that the basemap in Figure 3 is a mesh of various resolutions, and not a good indicator of visible albedo at low resolution.) This transition occurs near 0 W and 180 W, consistent with global patterns of sulfur bombardment and electron irradiation (Dalton et al. 2013). This is further evidence for the distinct nature of the dominant hydrates between the leading and trailing hemisphere, and may serve as a clue for a future spectral modeling investigation.

Laboratory spectra of several candidate surface species are shown with the observed spectra in Figure 2. Following Carlson et al. (2009), we digitize their sulfuric acid octahydrate spectrum and include epsomite and blödite from the USGS spectral library, which were obtained at room temperature. We also plot the spectra of irradiated NaCl evaporite and irradiated KCl grains measured at 100 K (K. P. Hand et al. 2016, in preparation). These anhydrous and evaporite spectra show 3 and 4.5 μm bands and are due to small amounts of residual water. We note that their absolute reflectance is much higher than the observed spectra, which would indicate additional water or other darkening agents. The NaCl spectrum is a particularly good match in shape and peak wavelength to the observed chaos region spectra. The blödite and epsomite spectra peak at longer wavelengths but are a closer match in absolute reflectance, though the agreement may be better at low temperature. Importantly, all of the salty ice spectra show longward shifts of the 3.7 μm peak compared to pure water ice, as seen in the chaos region spectra compared to icy region spectra. Sulfuric acid has little spectral structure at these wavelengths, and remains the most probable non-ice composition for primarily the trailing hemisphere, and potentially a darkening agent for the entire surface. The possible step-like feature in the trailing hemisphere spectrum near 3.2 μm is similar to the feature in blödite, though the wavelengths of these features do not quite match, but may agree at low temperature, after irradiation, or in multiple component mixtures. We also note that the selection in Figure 2 represents the limited number of laboratory spectra available, although many spectra from the USGS and ASTER spectral libraries are clearly inconsistent with the observed spectra and are not shown. Though cryogenic optical constants are available for water ice (Mastrapa et al. 2009), we are aware of no other optical constants for candidate materials at these wavelengths, low temperatures, and necessary precision to justify a detailed spectral modeling investigation.

In summary, we have obtained spatially resolved reflectance spectra of Europa's surface at 3.1–4.0 μm, which is a significant improvement on previous spectra at these wavelengths. These spectra show distinct latitudinal and longitudinal variations consistent with known albedo and compositional geography. Specifically, leading hemisphere equatorial spectra show a stronger, shifted 3.7 μm peak relative to the water ice-rich regions, which may be a characteristic of Europa's endogenous salts. This behavior is consistent with laboratory spectra of irradiated NaCl and the chloride hypothesis (Brown & Hand 2013; Hand & Carlson 2015), though additional species are certainly present and more work is needed to confirm this hypothesis.

This research was supported by Grant 1313461 from the National Science Foundation and by the NASA Earth and Space Science Fellowship. K.P.H. acknowledges support from the Jet Propulsion Laboratory, California Institute of Technology, under a contract with the National Aeronautics and Space Administration. The data presented herein were obtained at the W. M. Keck Observatory, which is operated as a scientific partnership among the California Institute of Technology, the University of California, and the National Aeronautics and Space Administration. The Observatory was made possible by the generous financial support of the W. M. Keck Foundation. The authors wish to recognize and acknowledge the very significant cultural role and reverence that the summit of Maunakea has always had within the indigenous Hawaiian community. We are most fortunate to have the opportunity to conduct observations from this mountain.

REFERENCES

Astropy Collaboration, Robitaille, T. P., Tollerud, E. J., et al. 2013, A&A, 558, A33
Brown, M. E., & Hand, K. P. 2013, AJ, 145, 110
Brown, R. H., Clark, R. N., Buratti, B. J., et al. 2006, Sci, 311, 1425
Carlson, R. W., Anderson, M. S., Johnson, R. E., et al. 1999, Sci, 283, 2062
Carlson, R. W., Calvin, W. M., Dalton, J. B., et al. 2009, in Europa, ed. R. T. Pappalardo et al. (Tucson, AZ: Univ. Arizona Press), 283
Carr, M. H., Belton, M. J. S., Chapman, C. R., et al. 1998, Natur, 391, 363
Cassidy, T., Paranicas, C. P., Shirley, J. H., et al. 2013, P&SS, 77, 64
Clark, R. N., Cruikshank, D. P., Jaumann, R., et al. 2012, Icar, 218, 831
Clark, R. N., Swayze, G. A., Wise, R., et al. 2007, USGS Digital Spectral Library splib06a: U.S. Geological Survey, Digital Data Series, 231 http://speclab.cr.usgs.gov/spectral.lib06
Collins, G., & Nimmo, F. 2009, in Europa, ed. R. T. Pappalardo et al. (Tucson, AZ: Univ. Arizona Press), 259
Dalton, J. B., Cassidy, T., Paranicas, C., et al. 2013, P&SS, 77, 45
Doggett, T., Greeley, R., & Figueredo, P. H. 2009, in Europa, ed. R. T. Pappalardo et al. (Tucson, AZ: Univ. Arizona Press), 137
Emery, J. P., Burr, D. M., Cruikshank, D. P., Brown, R. H., & Dalton, J. B. 2005, A&A, 435, 353
Fischer, P. D., Brown, M. E., & Hand, K. P. 2015, AJ, 150, 164
Hand, K. P., & Brown, M. E. 2013, ApJL, 766, L21
Hand, K. P., & Carlson, R. W. 2015, GeoRL, 42, 3174
Hand, K. P., Carlson, R. W., & Chyba, C. F. 2007, AsBio, 7, 1006
Hansen, G. B., & McCord, T. B. 2008, GeoRL, 35, L01202
Hapke, B. 1981, JGR, 86, 3039
Lebofsky, L. A., & Feierberg, M. A. 1985, Icar, 63, 237
Lord, S. D. 1992, NASA Technical Memorandum, 103957
Lucchitta, B. K., & Soderblom, L. A. 1982, in Satellites of Jupiter, ed. D. Morrison (Tucson, AZ: Univ. Arizona Press), 521
Mastrapa, R. M., Sandford, S. A., Roush, T. L., Cruikshank, D. P., & Dalle Ore, C. M. 2009, ApJ, 701, 1347
McCord, T. B., Hansen, G. B., Clark, R. N., et al. 1998, JGR, 103, 8603
McLean, I. S., Becklin, E. E., Bendiksen, O., et al. 1998, Proc. SPIE, 3354, 566
Moore, J. M., Black, G., Buratti, B., et al. 2009, in Europa, ed. R. T. Pappalardo et al. (Tucson, AZ: Univ. Arizona Press), 283
Nicholson, P. D., Hedman, M. M., Clark, R. N., et al. 2008, Icar, 193, 182
Ockman, N. 1958, Advances in Physics, 7, 199
Pollack, J. B., Witteborn, F. C., Erickson, E. F., et al. 1978, Icar, 36, 271
Smythe, W. D., Carlson, R. W., Ocampo, A., et al. 1998, Lunar and Planetary Science Conf. XXIX, Absorption Bands in the Spectrum of Europa Detected by the Galileo NIMS Instrument, ed. W. D. Smythe et al. (Houston, TX: LPI), 1532
Spencer, J. R. 1987, Icar, 70, 99
van der Walt, S., Schoönberger, J. L., Nunez-Iglesias, J., et al. 2014, PeerJ, 2, e453